Journal of Coastal Research	SI	90	261-266	Coconut Creek, Florida	2019

Estimation of Satellite-Based Upper-Ocean Temperature Profile in the Western North Pacific and Its Application to Tropical Cyclone Intensity Predictions

You-Hyun Baek[†] and Il-Ju Moon[†*]

[†]Typhoon Research Center
Jeju National University
Jeju, Republic of Korea

www.cerf-jcr.org

www.JCRonline.org

ABSTRACT

Baek, Y.-H. and Moon, I.-J., 2019. Estimation of satellite-based upper-ocean temperature profile in the western North Pacific and its application to tropical cyclone intensity predictions, *In:* Jung, H.-S.; Lee, S.; Ryu, J.-H., and Cui, T. (eds.), *Advances in Remote Sensing and Geoscience Information Systems of Coastal Environments*. *Journal of Coastal Research*, Special Issue, No. 90, pp. 261-266. Coconut Creek (Florida), ISSN 0749-0208.

Satellite measurements have limitations in obtaining information below sea surface, because they assess only the ocean surface. However, combining the satellite-measured sea surface temperature and heights with a large number of ARGO and reanalysis profiles allows estimating upper-ocean temperature profiles (UTPs) below the surface. In this study, a satellite-based UTP estimation algorithm was developed using a massive data set of 128,136 ARGO profiles and ocean reanalysis data collected over 17 years (2000–2016). The algorithm has the advantage of producing UPTs in all tropical cyclone (TC)-passing areas in the western North Pacific (WNP) without missed points. The verification results revealed that the estimated UTPs and TC-intensity-related predictors, such as depth-averaged temperatures up to 80 m and 100 m, isothermal depths at 20 ℃ and 26 ℃, ocean heat content, and maximum potential intensity, overall are in good agreement with the observations, although there still exists a relatively large error in the higher latitudes (north of 40°N) and the Kuroshio extension area where spatial and temporal variations are large. Based on the relationships between the TC intensity change and the predictors obtained for WNP TCs during 2004–2014, this study finally provides a guideline for predicting satellite-based TC intensity using estimated predictors.

ADDITIONAL INDEX WORDS: *ARGO float, upper-ocean temperature profile, tropical cyclone, intensity prediction, satellite-measured sea surface temperature and height.*

INTRODUCTION

Upper-ocean temperature profiles (UTPs) in the top 200 to 300 m provide crucial information for the intensity prediction of tropical cyclones (TCs, or typhoons), because TCs interact with the ocean within this layer (Cione *et al.*, 2013; Holliday and Thompson, 1979; Leipper and Volgenau, 1972; Moon and Kwon, 2012). When a TC passes over the ocean, the upper ocean is mixed by TC-induced strong wind forcing, producing sea surface cooling through the entrainment (and/or upwelling) of the deeper cold water into the warm surface water (Bender and Ginis, 2000; Cione and Uhlhorn, 2003; Lin *et al.*, 2008; Kim, Moon, and Chu, 2018; Price, 1981). TC-induced cooling of the sea surface has a negative impact on the intensity of TCs, because the cooling reduces the enthalpy flux supply from the ocean to the TC. Today, UTPs are provided by numerical ocean models through data assimilations (Cummings and Smedstad, 2013; Mogensen *et al.*, 2009), but satellite-based UTPs are still widely used in operational forecasts (Goni *et al.*, 2009; Shay, Goni, and Black, 2000), as these UTPs ensure not only accuracy but also much faster calculation than numerical models.

The traditional method for estimating satellite-based UTPs was mainly based on a two-layer reduced gravity model, in which only two isotherms (*i.e.*, the depths of 20 ℃ and 26 ℃ isotherms, or D20 and D26) are derived to coarsely characterize the UTP using a sea surface height anomaly (SSHA) from satellites (Goni and Trinanes, 2003; Goni *et al.*, 2009; Pun *et al.*, 2007; Shay, Goni, and Black, 2000). Then, the linear regression method (LRM) improved the vertical resolution of satellite-derived UTPs by applying a large set (>38,000) of *in situ* Array for Real-time Geostrophic Oceanography (ARGO) temperature profiles observed during 2000–2008 to regression development (Pun, Lin, and Ko, 2014). The LRM derives continuous isotherms from the depths of 4 ℃ (D4) to those of 29 ℃ (D29) (a maximum of 26 subsurface layers) to characterize the UTP in detail.

Although the LRM has produced high-accuracy UTPs for predicting typhoon intensity in the western North Pacific (WNP), the LRM cannot produce UTPs in places without ARGO data, such as the East China Sea (ECS), the Yellow Sea (YS), and the South China Sea (SCS), although TCs often pass through these seas (see Figure 1). In particular, most typhoons making landfall in Asian countries, including South Korea and China, pass through these seas where UTPs are not produced (Figure 1A). This makes it difficult to apply existing methods to predict the intensity of typhoons in these countries. In addition, the LRM has been verified only for peak TCseasons, from May to

DOI: 10.2112/SI90-032.1 received 1 April 2019; accepted in revision 13 June 2019.
*Corresponding author: ijmoon@jejunu.ac.kr

October, although TCs are generated in other seasons (Pun, Lin, and Ko, 2014).

This study aims to develop an all-season satellite-based UTP estimation algorithm for all typhoon-passing regions in the WNP (Figure 1A). For regions where ARGO data do not exist or are not enough, ocean reanalysis data that are produced from numerical assimilations using various ocean observation data are used, in addition to ARGO data. The present study uses a much larger set of ARGO profiles (>120,000), which have been accumulated over a long-term period (2000–2016), than the existing LRM (>38,000), and the larger data set will allow for more robust UTP estimation. Finally, this study estimates various predictors related to TC intensity using the calculated UTP data, and provides a guideline for applying these predictors to operational forecasts for TC intensity in the WNP region.

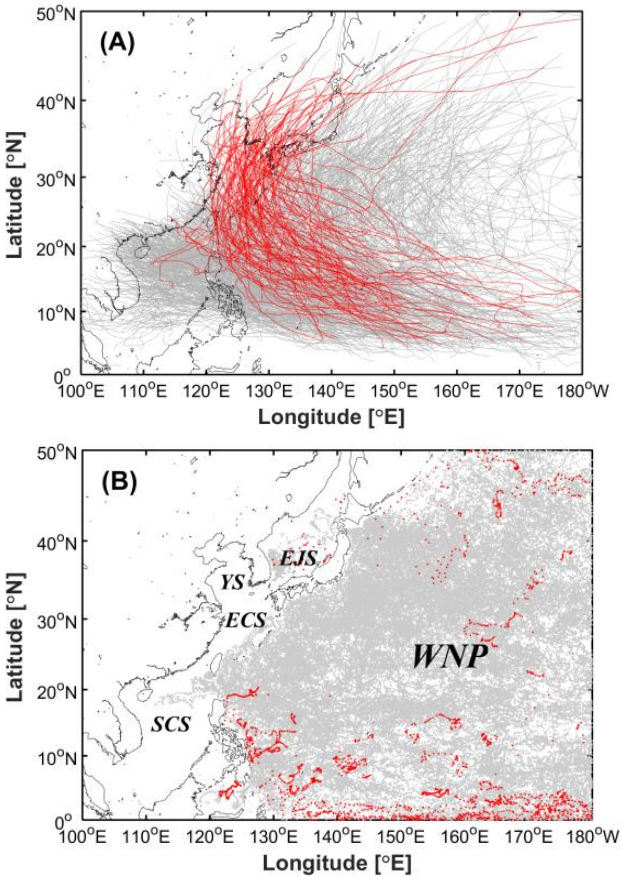

Figure 1. (A) Distribution of TC tracks (gray line) over the WNP from 1979 to 2016. Red lines indicate TCs that affected the Korean peninsula. (B) Locations of ARGO floats used in the present study. Gray dots represent the location of floats (a total of 120,096) to calculate linear regression coefficients during the training period (2000–2014), and red dots represent the location of floats (a total of 8,040) used during the verification period (2015–2016).

METHODS

The satellite-observed SSHA reflects the characteristics of the upper-ocean temperature, because the effect of thermal expansion is mostly much greater than that of saline contraction (Gill and Niiler, 1973). In particular, as the intraseasonal variations in the deep ocean temperature are small, a positive (negative) SSHA indicates warm (cold) water mass or a deep (shallow) mixed layer in the upper ocean (Pun *et al.*, 2007). Therefore, anomalies (ΔD_i) in the depth (D_i) with a certain water temperature ($_i$) from the climatology value ($\overline{D_i}$) at a certain ARGO point are larger in the positive SSHA region than in the negative SSHA region. Based on this assumption, UTPs are estimated from the relationship (equation 1) between the SSHA and ΔD_i (*i.e.*, ARGO-estimated D_i − climatological D_i) using all ARGO profiles (120,096 for 2000–2014) measured at every 0.25° × 0.25° (about 25 km) moving-window grid on a monthly basis (see Figure 2).

$$\Delta D_{i,x,y,t} = a(i,x,y,m) \times \eta_{i,x,y,t} + b(i,x,y,m) \qquad (1)$$

where η is the satellite-observed SSHA; a and b are the linear regression coefficients representing the slope and the offset, respectively, in which both are a function of location (x, y; interval of 0.25°); i is the isotherm (D4–D29) of 26 layers from 4 °C to 29 °C; m is the month from January to December; and t is the day.

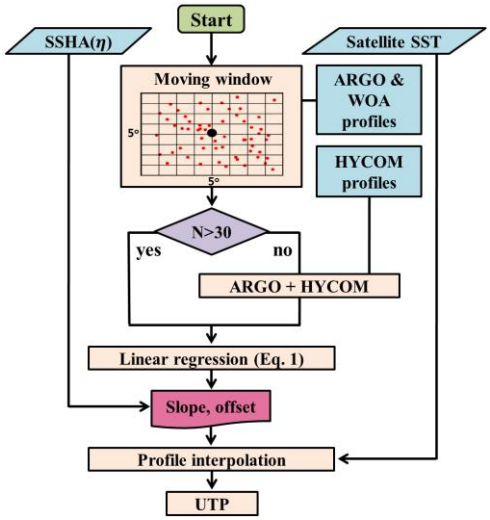

Figure 2. A flowchart for estimating satellite-based UTPs. To obtain a robust and statistically significant regression based on a large number of ARGO profiles, a moving-window approach with all profiles within a window of 5° longitude by 5° latitude centered at the grid is used. For the regions where the number of ARGO profiles is less than 30 at each grid, ocean reanalysis data are also used. Based on the calculation of the regression coefficients (the slope and the offset) for 2000–2014, the UTPs using the satellite-derived sea surface temperature (SST) and SSHA, in which the SST is combined with the profiles from 4 °C to 29 °C estimated by the regression, are calculated.

Table 1. *Descriptions of data sets used to estimate the satellite-based UTPs.*

Name	Descriptions	Temporal Resolution	Spatial Resolution	Data Type
SSHA	Copernicus (AVISO) MSLA-L4 SSHA	Daily	0.25°	Gridded
SST	RSS-MW OI L4 SST	Daily	0.25°	Gridded
Ocean Temp. Profiles	ARGO profile delayed mode	Monthly collection	5°×5°	
	HYCOM/NCODA	Daily	1/12°	Gridded
	World Ocean Atlas 2013	Daily	0.25°	Gridded
Atmospheric Temp./ Humidity Profiles	GFS	6h	1°	Gridded

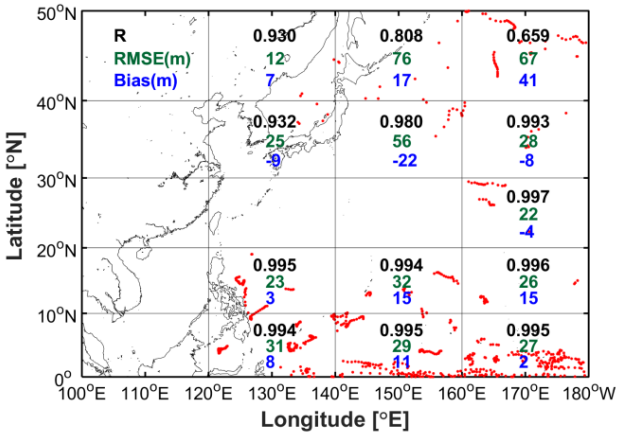

Figure 3. Spatial distributions of R (black), RMSE (green), and bias (blue) for the estimated UTPs during 2015–2016. Statistical analyses are performed for 20° (x-axis) × 10° (y-axis) grids. Red dots indicate the locations of the ARGO profiles (2015–2016) used for the verification.

ARGO profiles, which are delayed-mode data after quality control (QC) procedures, are obtained from the ARGO data center (http://www.argo.net; ARGO, 2013). The profiles are used for training (2000–2014) and verification (2015–2016) periods. Ocean reanalysis data are used to calculate UTPs for the places without ARGO observations, as well as for the relationship between TC-intensity-related predictors and changes in TC intensity. The reanalysis data are from the Hybrid Coordinate Ocean Model/Navy Coupled Ocean Data Assimilation (HYCOM/NCODA) system (https://www.hycom.org). To calculate the TC-intensity-related predictors, atmospheric temperature and humidity profiles from Global Forecasting System (GFS) reanalysis data (https://www.ncdc.noaa.gov/data-access/model-data/model-datasets/global-forcast-system-gfs) are also used.

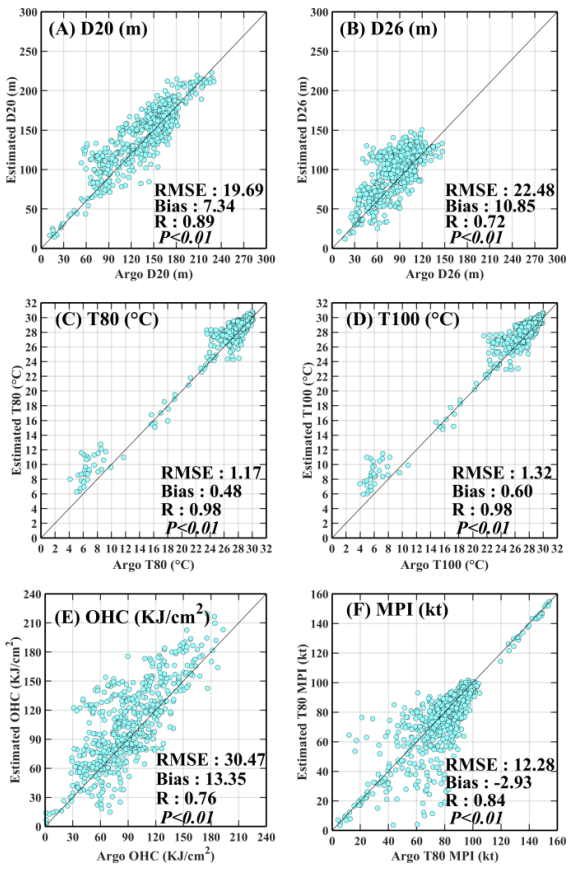

Figure 4. Scatter plots of the estimated predictors (A, D20; B, D26; C, T80; D, T100; E, OHC; and F, MPI), which are related to the typhoon intensity, compared with the ARGO observations. RMSE, R (with significance level), and bias with respect to the ARGO data are denoted in the lower-right corner.

Climatological mean UTPs are obtained from World Ocean Atlas (WOA) 2013 data (https://www.nodc.noaa.gov/OC5/woa13/woa13data.html). The best track TC data in the WNP are from the Joint Typhoon Warning Center (JTWC) (http://www.metoc.navy.mil/jtwc/jwwc.html). The TCs that affected the Korean peninsula (KP) are determined by the definition of the National Typhoon Center (KMA, 2011). SSHA and SST data for 2000–2016 are obtained from the Copernicus Level 4 products (http://marine.copernicus.eu) and the RSS-MW OI L4 SST (http://www.remss.com), respectively, in which the spatial and temporal resolutions are 0.25° and daily. Information about all input data used in this study is listed in Table 1.

Once the UTPs are calculated via the procedure shown in Figure 2, TC-intensity-related predictors, such as the ocean heat content (OHC), maximum potential intensity (MPI), intensification potential (POT), ocean temperatures averaged from the surface to 80-m and 100-m depths (T80, T100), and

isothermal depths at 20 °C and 26 °C (D20, D26), are estimated. The OHC is well-known as an oceanic predictor that explains the upper-ocean thermal structure, and is expressed as the product of the density, specific heat capacity, and the volume integral of the temperature above 26 °C from surface (sfc):

$$\mathrm{OHC} = C_p \rho \int_{sfc.}^{D26} (T - 26) dz, \quad (2)$$

where C_p is the seawater-specific heat capacity ($C_p = 4.186 Jkg^{-1}K^{-1}$), ρ is the water density ($\rho = 1024 kgm^{-3}$), D26 is the 26ºC isothermal depth, and T is the ocean temperature at a specific depth.

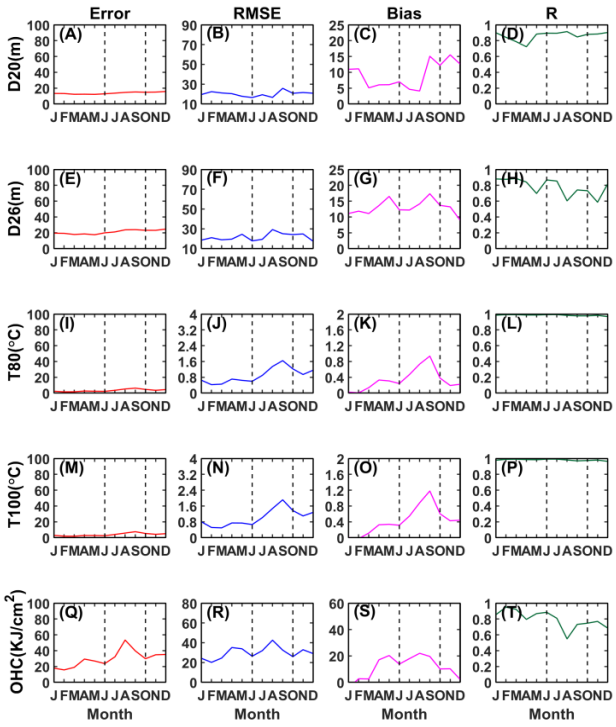

Figure 5. Monthly variations in the error (1st column), RMSE (2nd column), bias (3rd column), and R (4th column) for the estimated D20 (A-D), D26 (E-H), T80 (I-L), T100 (M-P), and OHC (Q-T) during 2015–2016. Dashed lines represent the peak TC seasons (JJASO).

T80 and T100 are depth-averaged temperatures, which are known to be better predictors of changes in TC intensity than the widely used OHC (Price, 2009). The MPI is the upper bound of the TC intensity given the atmospheric vertical profiles and depth-averaged temperatures (Emanuel 1988; Lin *et al.*, 2013):

$$\mathrm{MPI} = \frac{\bar{T} - T_0}{T_0} \frac{C_k}{C_D} (k^* - k), \quad (3)$$

where $\bar{T}$ is the 80-m depth-averaged ocean temperature (T80), $T_0$is the TC outflow temperature determined by the atmospheric vertical profile, C_D is the drag coefficient, C_k is the enthalpy exchange coefficient, and $k^*$and k are the saturation enthalpy of the sea surface and the surface enthalpy in the TC environment, respectively.

Intensification potential (POT) is the TC potential future intensity changes (DeMaria and Kaplan, 1994), defined as the difference between MPI and maximum wind at the initial time.

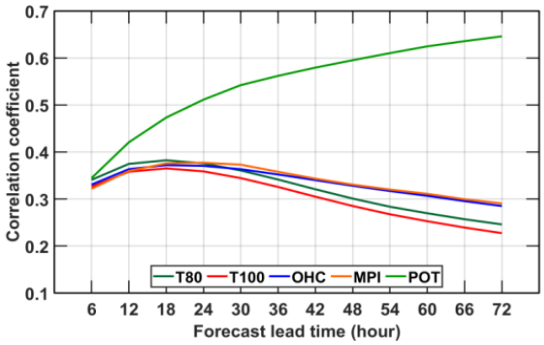

Figure 6. The correlation coefficients between five predictors (T80, T100, OHC, MPI, and POT) and the change in the TC intensity according to the forecast lead time (6-h intervals).

RESULTS

The 8,040 ARGO profiles in 2015 and 2016 were used to validate the UTPs estimated from the proposed algorithm. The locations of these profiles are shown in Figure 1B (see the red dots). For validation, root mean square errors (RMSEs), biases, correlation coefficient (R), and Errors (defined as the percentage of RMSE in the observed mean) between the observed (*i.e.*, ARGO profiles) and estimated UTPs were calculated at all depths, and averaged over 20° × 10° grid boxes (Figure 3). It can be seen that the UTPs are well reproduced in most regions where TCs frequently pass (RMSE < 33 m and R > 0.99) except the East Sea, north of 40°N, and the Kuroshio extension area where spatial and temporal variations are large due to the encounter of warm and cold currents.

In addition to the UTP, six TC-intensity-related predictors are calculated and validated. These parameters are D20, D26, T80, T100, OHC, and MPI (Figure 4). For D20 and D26, the RMSEs (R) were 19.7 m (0.89) and 22.5 m (0.72), respectively, suggesting that the performance of D20 is slightly better than that of D26. For T80 and T100, the RMSEs (R) are 1.2 °C (0.98) and 1.3 °C m (0.98), respectively. These results are comparable with or superior to those of state-of-the-art numerical models (Ko *et al.*, 2018). The estimated OHC and MPI showed a reasonable performance with the RMSEs of 30.5 KJ/cm^2 and 12.3 kt.

To examine seasonal variations in the performance, the estimated D20, D26, T80, T100, and OHC are validated according to the month (Figure 5).

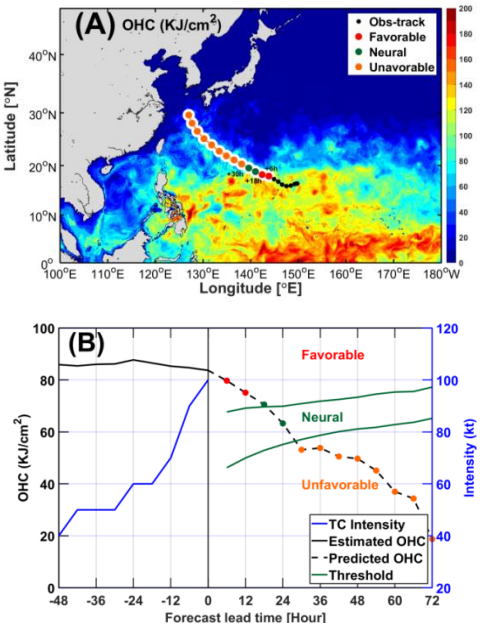

Figure 7. An example of the application of the estimated OHCs, which are calculated according to the forecast lead time (6-h interval), to the operational forecasts of TC intensity. (A) Spatial distribution of the OHC at the forecast time along the TC track with TC-development conditions (black dots, observed track; colored dots, predicted track). (B) Time series of the estimated OHCs, which are averaged within a 200-km radius from the storm center, along the observed track (red line with black dots) and the predicted track (dashed lines with colored dots). Red, green, and dark-yellow colors represent favorable, neutral, and unfavorable conditions for TC development, respectively. The two green lines represent the thresholds of the three conditions. The blue line represents the observed TC intensity.

The results reveal that the performance of all parameters varies with the season, that is, low in warmer seasons and high in colder seasons. The low performance in warmer seasons may be associated with the increased vertical temperature gradient and stratification due to strong surface heating during the warmer seasons, which produces the large variability in the temperature profiles and makes the accurate estimation of profiles difficult (Ko *et al.*, 2018).

To apply the estimated TC-intensity-related parameters to an operational TC forecast, their correlations with the change in TC intensity according to the forecast lead time must be calculated. The correlation coefficients for individual predictors (the T80, T100, OHC, MPI, and POT) were calculated for all WNP TCs during 2004–2014 (Figure 6). All predictors are averaged within a 200-km radius from the storm center. The results show that the correlations of all predictors, except the POT, increase until about the 24-h lead time, but decrease thereafter. For the POT, the correlation continuously increases as the forecast lead time increases, reaching 0.64 at 72-h lead time. The POT is considered the most important predictor in statistical TC intensity models (DeMaria and Kaplan, 1999; Kim, Moon, and Chu, 2018). This analysis also shows that the POT has the highest correlations with the intensity changes for all lead times (Figure 6).

Figure 7 shows an example of the application of the estimated OHCs to the operational TC intensity forecasts. The OHC is calculated at the forecast time, and the TC-development conditions (favorable, neutral, and unfavorable) are expressed along the predicted TC track (Figure 7A). The conditions are classified using the probability density function (PDF) between the intensity changes and the predictors, in which the neutral condition corresponds to $-0.5\sigma < PDF < 0.5\sigma$ (33.3 %) where σ is the standard deviation. Unfavorable and favorable conditions correspond to less than -0.5σ and more than $+0.5\sigma$, respectively. Based on these thresholds, the example TC will intensify until the +15-h lead time, maintain strength until +24 h, and then weaken (Figure 7B).

DISCUSSION

This study showed an example of the application of an estimated predictor to operational forecasts of TC intensity with a guideline for satellite-based TC intensity estimation, demonstrating that the present satellite-based UTP estimation algorithm is useful for predicting TC intensity. However, it has limitations in accurately predicting UTPs and their products in areas with large spatial and temporal variations. In particular, in coastal regions (*i.e.*, river plume areas) where the effect of salinity is important, the errors will increase, because the proposed methods assume that the satellite-observed SSHA reflects only thermal expansion. The future research will focusing on improving the present algorithm by acquiring more observational data, increasing the resolution of moving windows, and considering the effect of salinity.

CONCLUSIONS

During the passage of TCs, strong winds induce vertical mixing and upwelling, resulting in sea surface cooling, and thus, affecting the TC intensity. Therefore, the intensity of TCs is influenced not only by pre-storm SST conditions but also by subsurface thermal structures under the TC. Recently, it has become possible to indirectly estimate the thermal structure of the upper ocean using satellite SSHA data. Satellite-based UTP estimation is widely used in many operational agencies, because it can significantly reduce computational time compared to numerical models, and ensure high accuracy.

The present study developed an algorithm to calculate UTPs in the WNP based on satellite-produced SSHA and SST data, as well as various *in-situ* temperature profiles. The new algorithm has the advantage of estimating UTPs without missing a point for the entire WNP TC region by simultaneously using a massive data set of 128,136 ARGO profiles and ocean reanalysis data collected over 17 years (2000–2016), unlike previous studies that used limited observational data, and thus, produced UTPs only for regions where ARGO data exist.

Daily UTPs estimated by the present algorithm are compared with the ARGO data during 2015–2016, which were not used to develop the algorithm. The results reveal that most of the estimated UTPs agreed well with the observations, but a relatively large error still existed in the higher latitudes (north of

40°N) and the Kuroshio extension area, where the spatial and temporal variations are large. Using the estimated UTPs, six TC-intensity-related predictors (D20, D26, T80, T100, OHC, and MPI) were calculated and validated. The results show that the estimated predictors overall were in good agreement with the observations, varying with the season (that is, low in warmer seasons and high in colder seasons). In particular, two depth-averaged temperatures (T80 and T100), which are known to be better predictors for changes in TC intensity than the widely used OHC, showed the best agreement with the observations among all predictors.

ACKNOWLEDGMENTS

This work was supported by the “Development of Typhoon and ocean applications” project, funded by ETRI, which is a subproject of “Development of Geostationary Meteorological Satellite Ground Segment (NMSC-2018-01)” program funded by the National Meteorological Satellite Center (NMSC) of the Korea Meteorological Administration (KMA) and by the project titled "Construction of Ocean Research Stations and their Application Studies" funded by the Ministry of Oceans and Fisheries, Korea.

LITERATURE CITED

ARGO, 2013. *Argo Quality Control Manual Version 2.9*. http://www.argodatamgt.org/content/download/20685/142877/file/argo-quality-control-manual_version2.9.pdf.

Bender, M.A. and Ginis, I., 2000. Real-case simulations of hurricane–ocean interaction using a high-resolution coupled model: effects on hurricane intensity. *Monthly Weather Review,* 128(4), 917-946.

Cione, J.; Kalina, E.; Zhang, J., and Uhlhorn, E., 2013. Observations of air-sea interaction and intensity change in hurricanes. *Monthly Weather Review*, 141(7), 2368-2382.

Cione, J. and Uhlhorn, E., 2003. Sea surface temperature variability in hurricanes: implications with respect to intensity change. *Monthly Weather Review*, 131(8), 1783-1796.

Cummings, J.A. and Smedstad, O.M., 2013. Variational data assimilation for the global ocean. *Data Assimilation for Atmospheric, Oceanic and Hydrologic Applications,* 2, 303-343.

DeMaria, M. and Kaplan, J., 1994. Sea surface temperature and the maximum intensity of Atlantic tropical cyclones. *Journal of Climate*, 7(9), 1324-1334.

DeMaria, M. and Kaplan, J., 1999. An updated statistical hurricane intensity prediction scheme (SHIPS) for the Atlantic and eastern North Pacific basins. *Weather and Forecasting*, 14(3), 326-337.

Emanuel, K.A., 1988. The Maximum intensity of hurricanes. *Journal of the Atmospheric Sciences*, 45(7), 1143-1155.

Gill, A.E. and Niller, P.P., 1973. The theory of the seasonal variability in the ocean. *Deep-sea research*, 20(2), 141-177.

Goni, G.J.; Demaria, M.; Knaff, J.; Sampson, C.; Ginis, I.; Bringas, F.; Mavume, A.; Lauer, C.; Lin, I.I.; Ali, M.M.; Sandery, P.; Ramos-Buarque, S.; Kang, K.; Mehra, A.; Chassignet, E., and Halliwell, G., 2009. Applications of satellite-derived ocean measurements to tropical cyclone intensity forecasting. *Oceanography*, 22(3), 190-197.

Goni, G.J. and Trinanes, J.A., 2003. Ocean thermal structure monitoring could aid in the intensity forecast of tropical cyclones. *Eos Transactions American Geophysical Union*, 84(51), 573-580.

Holliday, C.R. and Thompson, A.H., 1979. Climatological characteristics of rapidly intensifying typhoons. *Monthly Weather Review*, 107(8), 1022-1034.

Kim, S.H.; Moon, I.J., and Chu, P.S., 2018. Statistical–dynamical typhoon intensity predictions in the Western North Pacific using track pattern clustering and ocean coupling predictors. *Weather and Forecasting*, 33(1), 347-365.

Ko, E.B.; Moon, I.J.; Jeong, Y.Y., and Chang, P.H., 2018. A comparison of accuracy of the ocean thermal environments using the daily analysis data of the KMA NEMO/NEMOVAR and the US Navy HYCOM/NCODA. *Atmosphere*, 28(1), 99-112.

Korean Meteorological Administration (KMA), 2011. *Typhoon White Book.* Seoul: Korean Meteorological Administration, 342p.

Leipper, D.F. and Volgenau, D., 1972. Hurricane heat potential of the Gulf of Mexico. *Journal of Physical Oceanography*, 2, 218-224.

Lin, I.I.; Black, P.; Price, J.F.; Yang, C.Y.; Chen, S.S.; Lien, C.C.; Harr, P.A.; Chi, N.H.; Wu, C.C., and D’Asaro, E.A., 2013. An ocean cooling potential intensity index for tropical cyclones. *Geophysical Research Letters*, 40(9), 1878-1882.

Lin, I.I.; Wu, C.C.; Pun, I.F., and Ko, D.S., 2008. Upper-ocean thermal structure and the western North Pacific category 5 typhoons. Part I: Ocean features and the category 5 typhoons’ intensification. *Monthly Weather Review*, 136(9), 3288-3306.

Mogensen, K.; Balmaseda, M.A.; Weaver, A.T.; Martin, M., and Vidard, A., 2009. NEMOVAR: A variational data assimilation system for the NEMO model. *European Centre for Medium-Range Weather Forecasts Newsletter*, 120, 17-22.

Moon, I.J. and Kwon, S.J., 2012. Impact of upper-ocean thermal structure on the intensity of Korean peninsula landfall typhoons. *Progress in oceanography*, 105, 61-66.

Price, J.F., 1981. Upper ocean response to a hurricane. *Journal of Physical Oceanography*, 11(2), 153-175.

Price, J.F., 2009. Metrics of hurricane–ocean interaction: vertically-integrated or vertically-averaged ocean temperature? *Ocean Science*, 5(3), 351-368.

Pun, I.F; Lin, I.I., and Ko, D.S., 2014. New generation of satellite-derived ocean thermal structure for the Western North Pacific typhoon intensity forecasting. *Progress in Oceanography*, 121, 109-124.

Pun, I.F.; Lin, I.I.; Wu, C.R.; Ko, D.H., and Liu, W.T., 2007. Validation and application of altimetry-derived upper ocean thermal structure in the western North Pacific Ocean for typhoon-intensity forecast. *Geoscience and Remote Sensing*, 45(6), 1616-1630.

Shay, L.K.; Goni, G.J., and Black, P.G., 2000. Effects of a warm oceanic feature on Hurricane Opal. *Monthly Weather Review,* 128(5), 1366-1383.